arXiv:2109.06743v2 [physics.plasm-ph] 21 Sep 2021

An Energy Conserving Vlasov Solver That Tolerates Coarse Velocity Space Resolutions: Simulation of MMS Reconnection Events

F. Allmann-Rahn[1], S. Lautenbach[2], R. Grauer[1]

[1] Institute for Theoretical Physics I, Ruhr-University Bochum, Germany

[2] Department of Physics, University of Alberta, Edmonton, Alberta T6G 2E1, Canada

Abstract

Vlasov solvers that operate on a phase-space grid are highly accurate but also numerically demanding. Coarse velocity space resolutions, which are unproblematic in particle-in-cell (PIC) simulations, can lead to numerical heating or oscillations in standard continuum Vlasov methods. We present a new dual Vlasov solver which is based on an established positivity preserving advection scheme for the update of the distribution function and an energy conserving partial differential equation solver for the kinetic update of mean velocity and temperature. The solvers work together via moment fitting during which the maximum entropy part of the distribution function is replaced by the solution from the partial differential equation solver. This numerical scheme makes continuum Vlasov methods competitive with PIC methods concerning computational cost and enables us to model large scale reconnection in Earth's magnetosphere with a fully kinetic continuum method. The simulation results agree well with measurements by the MMS spacecraft.

1 Introduction

In many plasmas, for example the space plasma around the Earth and the sun and plasmas in fusion devices, collisions are rare. Therefore kinetic methods are necessary to accurately model these plasmas. Kinetic continuum Vlasov simulations provide an accurate and noise-free representation of velocity space, but solve the Vlasov equation on a phase space grid which is numerically challenging. In order to avoid unphysical negative values for the particle distribution function, positivity preserving limiters can be introduced. These, however, lead to numerical heating of the plasma so that conservation of total energy is violated. In Vlasov solvers that conserve energy, on the other hand, special care must be taken to keep numerical oscillations (caused by negative values of the distribution function) under control. Otherwise, their usability over longer time-spans is limited in simulations with prominent non-linear effects. Both numerical heating and non-positivity become more problematic at low resolutions/large cell sizes in velocity space. Published full Vlasov simulations of magnetic reconnection (e.g. Schmitz and Grauer [2006a], Pezzi et al. [2019, 2021], Liu et al. [2021]) did not go beyond the GEM reconnection setup [Birn et al., 2001] which is computationally manageable due to the small system size.

To give an overview, we want to mention just a few of the many available schemes for solving the Vlasov equation on a phase-space grid, together with related implementations in high-performance computing codes. The pioneer work of Cheng and Knorr [1976] used a semi-Lagrangian approach with spline or Fourier interpolation. A high-performance implementation that uses Lagrange interpolation can be found in Kormann et al. [2019]. Such semi-Lagrangian solvers are still most popular due to their computational efficiency. Here, we use the third-order semi-Lagrangian positive and flux-conservative (PFC) scheme in Filbet et al. [2001] which ensures positivity of the distribution function and conserves mass and fluxes. A similar approach with higher-order accuracy can be found in Tanaka et al. [2017]. The PFC scheme was first applied to magnetic reconnection in Schmitz and Grauer [2006a]. More recently, discontinuous Galerkin methods were adopted for Vlasov simulations e.g. a semi-Lagrangian approach in Rossmanith and Seal [2011]. A discontinuous Galerkin scheme with Runge-Kutta time integration, implemented for the full Vlasov-Maxwell system, is given in Juno et al. [2018] and Hakim and Juno [2020]. This scheme

Corresponding author: Florian Allmann-Rahn, far@tp1.rub.de

conserves total energy, and although it does not preserve positivity of the distribution function, the plasma turbulence simulation in Juno et al. [2018] was not impaired by numerical oscillations.

Magnetic reconnection is a fundamental energy conversion process in plasmas throughout the universe and can excite instabilities in fusion devices. In 2015 the Magnetospheric Multiscale Mission (MMS) spacecraft was launched to directly measure reconnection in the Earth's magnetosphere [Burch et al., 2016]. There have been successful comparisons between simulations of reconnection using fully kinetic particle-in-cell (PIC) models and MMS measurements [Nakamura et al., 2018, Liu et al., 2020, Lu et al., 2020]. In the particle-in-cell (PIC) method the velocity space is represented by super-particles, which represent a large amount of actual particles, using a Monte-Carlo approach. This is very efficient because the method is stable and produces reasonable results even at low velocity space resolution (i.e. low numbers of particles) and in many cases the number of particles is higher in regions of interest so that the simulation accuracy adapts nicely to the physical configuration. However, when too few particles are used, discrete particle noise can limit simulation accuracy [Nevins et al., 2005, Juno et al., 2020]. Both the continuum Vlasov method and the PIC method have their respective strengths, but the primary reason that continuum solvers could so far not compete with PIC is the numerical difficulty of treating low velocity space resolutions.

In this paper we present a method to make a Vlasov solver both positivity preserving and energy conserving by means of moment fitting. This relaxes the numerical necessity of high velocity space resolutions and thus enables us to address large-scale problems with a fully kinetic continuum solver. We show in comparisons between reconnection simulations and MMS measurements that the Vlasov method can provide an accurate representation of the electric field at moderate computational cost.

2 Physical and Numerical Models

2.1 The Vlasov-Maxwell System and its Numerical Representation

A collisionless plasma evolves according to the Vlasov equation

$$\frac{\partial f_s}{\partial t} + \mathbf{v} \cdot \nabla f_s + \frac{q_s}{m_s}(\mathbf{E} + \mathbf{v} \times \mathbf{B}) \cdot \nabla_v f_s = 0, \tag{1}$$

where $f_s(\mathbf{x}, \mathbf{v}, t)$ is the particle distribution function for each species s. A collision operator can be added to the right hand side of the equation in the case of collisional plasmas. From the distribution function physical quantities can be obtained by taking moments. The particle density is given by $n_s(\mathbf{x}, t) = \int f_s(\mathbf{x}, \mathbf{v}, t)\mathrm{d}\mathbf{v}$ and the mean velocity is $\mathbf{u}_s(\mathbf{x}, t) = \frac{1}{n_s(\mathbf{x},t)} \int \mathbf{v} f_s(\mathbf{x}, \mathbf{v}, t)\mathrm{d}\mathbf{v}$. The second and third moment (multiplied by mass) are momentum flux density $\mathcal{P}_s = m_s \int \mathbf{v} \otimes \mathbf{v} f_s \mathrm{d}\mathbf{v}$ and energy flux density $\mathcal{Q}_s = m_s \int \mathbf{v} \otimes \mathbf{v} \otimes \mathbf{v} f_s \mathrm{d}\mathbf{v}$, respectively, where $\otimes$ denotes the tensor (outer) product. Heat flux Q is related to the third moment $\mathcal{Q}$ like $\mathrm{Q}_{ijk} = \mathcal{Q}_{ijk} - \mathrm{sym}(\mathbf{u} \otimes \mathcal{P})_{ijk} + 2mnu_iu_ju_k$ and temperature T to the second moment $\mathcal{P}$ like $\mathrm{T}_{ij} = (\mathcal{P}_{ij} - mnu_iu_j)/(nk_B)$. From the heat flux tensor the heat flux vector can be obtained as $\mathbf{q}_i = \sum_j \mathrm{Q}_{ijj}$.

Taking moments of the complete Vlasov equation, a set of fluid equations follows:

$$\frac{\partial n_s}{\partial t} + \nabla \cdot (n_s \mathbf{u}_s) = 0\,, \tag{2}$$

$$m_s \frac{\partial (n_s \mathbf{u}_s)}{\partial t} = n_s q_s (\mathbf{E} + \mathbf{u}_s \times \mathbf{B}) - \nabla \cdot \mathcal{P}_s\,, \tag{3}$$

$$\frac{\partial \mathcal{P}_s}{\partial t} - q_s (n_s \mathrm{sym}(\mathbf{u}_s \otimes \mathbf{E}) + \frac{1}{m_s} \mathrm{sym}(\mathcal{P}_s \times \mathbf{B})) = -\nabla \cdot \mathcal{Q}_s\,. \tag{4}$$

Here, sym is the symmetrization, i.e. the sum over permutations of indices to make the tensors symmetric, for example $\mathrm{sym}(\mathbf{u} \otimes \mathbf{E})_{ij} = u_iE_j + u_jE_i$, and the vector product $\times$ is generalized to tensors.

The fluid equations are exact but contain more unknowns than equations, in particular there is no equation for $\mathcal{Q}_s$. In the moment fitting Vlasov method we obtain $\mathcal{Q}_s$ directly from the distribution function so that the fluid equations are equivalent with the Vlasov equation. Multi-fluid methods instead make an approximation with a physically motivated closure expression as described in Sec. 2.3.

The evolution of electric and magnetic fields is determined by Maxwell's equations

$$\nabla \cdot \mathbf{E} = \frac{\rho}{\epsilon_0}\,, \quad \nabla \cdot \mathbf{B} = 0\,, \quad \nabla \times \mathbf{E} = -\frac{\partial \mathbf{B}}{\partial t} \quad \text{and} \quad \nabla \times \mathbf{B} = \mu_0 \mathbf{j} + \mu_0 \epsilon_0 \frac{\partial \mathbf{E}}{\partial t}\,.$$

Together with the Vlasov equation they form the Vlasov-Maxwell system of equations which fully describes the plasma dynamics.

In the electromagnetic simulations we normalize length over ion inertial length $d_{i,0}$ based on density n_0, velocity over ion Alfvén velocity $v_{A,0}$ based on the magnetic field B_0, time over the inverse of the ion cyclotron frequency $\Omega_{i,0}^{-1}$, mass over ion mass m_i, electric charge in ion charge q_i, and vacuum permeability $\mu_0 = 1$ as well as Boltzmann constant $k_B = 1$.

The Vlasov equation is solved by means of the PFC method in Filbet et al. [2001] and the velocity splitting is realized via the backsubstitution method [Schmitz and Grauer, 2006b]. We use zero-flux boundary conditions in velocity space to ensure conservation of particle density. The fluid solver utilizes a centrally weighted essentially non-oscillating (CWENO) method [Kurganov and Levy, 2000] and the third-order Runge-Kutta scheme in Shu and Osher [1988]. The finite-difference time-domain (FDTD) method is employed for the Maxwell equations.

The schemes were implemented in the *muphy2* multiphysics plasma simulation code developed at the Institute for Theoretical Physics I, Ruhr University Bochum. The framework part of the code is written in C++ whereas the pure computational parts are written in Fortran to benefit from its excellent performance when dealing with multi-dimensional arrays. Parallelization is done via domain decomposition and MPI. All solvers are fully ported to GPUs with highly optimized OpenACC. That way the same code base can be used for both GPU and CPU computations.

2.2 Moment Fitting for a Positive and Energy Conserving Vlasov Solver

As discussed, numerical solutions to the Vlasov equation (1) are not positivity preserving and energy conserving at the same time, whereas the fluid equations (2)–(4) are unproblematic in this regard. The idea for getting a both positive and energy conservative Vlasov solver is therefore to obtain the heat flux moment from the distribution function and use it in the fluid equations to get an exact kinetic solution to the Vlasov equation for the momentum and energy moments from the fluid solver. These moments are then used to update the maximum entropy part (in the Boltzmann sense) of the distribution function so that energy is conserved. We call this method *moment fitting*. The update of the distribution function is realized by calculating the ten-moment Maxwellian part of the distribution function and replacing it with the ten-moment Maxwellian calculated from the exact fluid solver moments. As density is conserved in both methods, this operation conserves the distribution function. Furthermore, it affects not more than the originally not conserved momentum and energy for which we now have numerically more accurate as well as kinetically correct solutions.

The original idea of moment fitting for improving Vlasov solvers is from Trost et al. [2017] and a simple form had been used before in Rieke et al. [2015] for spatial coupling of Vlasov and five-moment fluid models. Trost et al. [2017] adapted moments by shifting, stretching and rotating the distribution function. While that is certainly a good and successful approach, we want to address two subtleties that are involved. First, in that method the equation for determining the adaption of the distribution function is underdetermined and needs to be solved with a optimization algorithm under the additional constraint that the adaption is as close to unity as possible. Second, the whole distribution function is adapted and not only the part directly related to the maximum entropy ten-moment solution. That means also higher moments, which the fluid solver gives no kinetic solution for, are changed on basis of the new momentum and temperature. While this may often be desired, it is not clear that the result is in any case still a valid solution to the Vlasov equation. With the new method of exchanging only what the fluid solver gives definite answers to, we can be sure to not change the kinetic physics.

A time step of the moment fitting Vlasov solver as we have implemented it is shown in Algorithm 1. Since we use a semi-Lagrangian solver for the Vlasov equation and a Runge-Kutta solver for the Fluid equations, the Vlasov step is done first so that the third moment that the fluid solver needs is available at all Runge-Kutta times. Since the divergence of the third moment is needed in Eq. (4) it is incorporated into the CWENO reconstruction process. Concerning the moment fitting itself, we want to elaborate on some details. The maximum entropy distribution function based

Algorithm 1: Time stepping of the moment fitting Vlasov-Maxwell solver as it is implemented

1 **Time Step**
2 Half step of Maxwell solver
3 Calculate third moment $\mathcal{Q}^t$ from f^t
4 Full Vlasov Leapfrog Step to advance to f^{t+1}
5 Calculate $\mathcal{Q}^{t+1}$ from f^{t+1}
6 Interpolate to get $\mathcal{Q}^{t+1/2}$
7 Full Runge-Kutta Fluid Step (input $\mathcal{Q}$ at appropriate times)
8 **Moment Fitting**
9 Calculate moments n_V, $\mathbf{u}_\mathrm{V}$, $\mathcal{P}_\mathrm{V}$ from f
10 Calculate ten-moment Maxwellian $f_\mathrm{M,V}$ from n_V, $\mathbf{u}_\mathrm{V}$, $\mathcal{P}_\mathrm{V}$
11 Rescale the fluid solver's moments n_F, $\mathbf{u}_\mathrm{F}$, $\mathcal{P}_\mathrm{F}$ by $n_\mathrm{V}/n_\mathrm{F}$ to ensure conservation of f
12 Calculate ten-moment Maxwellian $f_\mathrm{M,F}$ from the fluid solver's moments
13 Exchange ten-moment Maxwellians: $f = f - f_\mathrm{M,V} + f_\mathrm{M,F}$
14 Limit f
15 **end**
16 Second half step of Maxwell solver
17 **end**

on density n, mean velocity $\mathbf{u}$ and temperature tensor $\mathrm{T} = \frac{m}{k_B n}\int(\mathbf{v}-\mathbf{u})\otimes(\mathbf{v}-\mathbf{u})f\mathrm{d}\mathbf{v}$, which we here call the ten-moment Maxwellian, is given by

$$f_M(\mathbf{x},\mathbf{v}) = n(\mathbf{x})\left(\frac{m}{2\pi k_B}\right)^{N/2}\exp\left(-\frac{m}{2k_B}(\mathbf{v}-\mathbf{u}(\mathbf{x}))^\mathrm{t}\ \mathrm{T}^{-1}\ (\mathbf{v}-\mathbf{u}(\mathbf{x}))\right)/\sqrt{\det\mathrm{T}(\mathbf{x})},$$

where $(\mathbf{v}-\mathbf{u})^\mathrm{t}$ is the transpose of $\mathbf{v}-\mathbf{u}$ and N is the dimensionality of velocity space. To have the distribution function conserved when exchanging the ten-moment Maxwellians, the respective densities must be identical. Both solvers conserve mass and solve the same equation so in principal they should also yield the same density. There are, however, small numerical errors which we compensate by rescaling the fluid moments by the density obtained from the distribution function (Alg. 1, line 11). That way we make sure that only unconserved quantities are changed during this step. Especially where the distribution function is close to zero, the exchange of the ten-moment Maxwellians can sometimes turn the value of the distribution function negative. In the simulations in this paper, we limit f by setting the respective values to zero in these cases (line 14) followed by a rescaling of the distribution function to the density before the exchange of the ten-moment Maxwellians. This may not be very elegant, but the good energy conservation properties discussed in the benchmark example sections justify the approach. Overall, the presented moment fitting method makes as few changes as possible to the distribution function when the full maximum entropy information on momentum and energy from the fluid solver is kept.

If the fluid scheme did additionally conserve total momentum, as shown e.g. in Balsara et al. [2016], the moment fitting would make the Vlasov solver conserve total momentum as well. So far it does at least improve the momentum conservation. The published momentum-conservative fluid solvers use five-moment models which make the physical simplification that $\mathrm{P} - \frac{1}{3}\mathrm{tr}(\mathrm{P})\,\mathrm{id} = 0$. Thus, they are not exact and cannot be used in the moment fitting method. The next step will be to transfer the ideas of available momentum-conservative fluid solvers to the ten-moment model which can then be utilized for a positivity preserving and mass, momentum and energy conserving Vlasov solver.

2.3 Fluid Solver with Gradient Heat Flux Closure

Ten-moment multi-fluid simulations close the hierarchy of equations with a heat flux approximation. Here, we use a modified version of the temperature gradient closure in Allmann-Rahn et al. [2018] and Allmann-Rahn et al. [2021]. The closure is based on the one-dimensional Landau fluid closure in Hammett and Perkins [1990] (also Hammett et al. [1992]) and takes inspiration from Wang et al. [2015]. Originally the gradient closure used the gradient of the pressure's deviation from isotropy. Instead, we now simply take the gradient of the temperature so that the heat flux approximation is given by

$$\nabla \cdot \mathrm{Q}_s = -\frac{\chi}{k_{s,0}}\, n_s\, v_{t,s}\, \nabla^2\, \mathrm{T}_s\,. \tag{5}$$

We choose $k_{s,0} = 1/d_s$ as the typical spatial frequency. The dimensionless parameter is $\chi = 2\sqrt{2/\pi}$ as in Hammett and Perkins [1990] and $v_{t,s} = \sqrt{\frac{k_B\ \mathrm{tr}(\mathrm{T}_s)/3}{m_s}}$ is the thermal velocity.

A closure that is similar to the one we use here can be found in Ng et al. [2020]. The only difference is that they employed a symmetrization in the process of generalizing the Landau fluid closure to three dimensions. The closure given by Eq. (5) yields in many cases more accurate results than the original formulation in Allmann-Rahn et al. [2018].

3 Benchmark Problems

3.1 Landau Damping and Two-Stream Instability

From a theoretical point of view, it is clear that the combination of a Vlasov and a fluid solver in the presented way yields correct solutions to the Vlasov equation (within the accuracy of the solvers). In this section we want to confirm at the example of standard tests for kinetic plasma solvers that this is indeed the case also numerically. In these test problems physical effects occur over short time spans and the resolution is high so that the standard PFC scheme does conserve energy and momentum precisely. That makes the setups ideal for verifying the moment fitting scheme which should yield identical results. No correction of the moments is to be expected but the Maxwellian part of the distribution function will still be fully handled by the fluid solver with kinetic heat flux input.

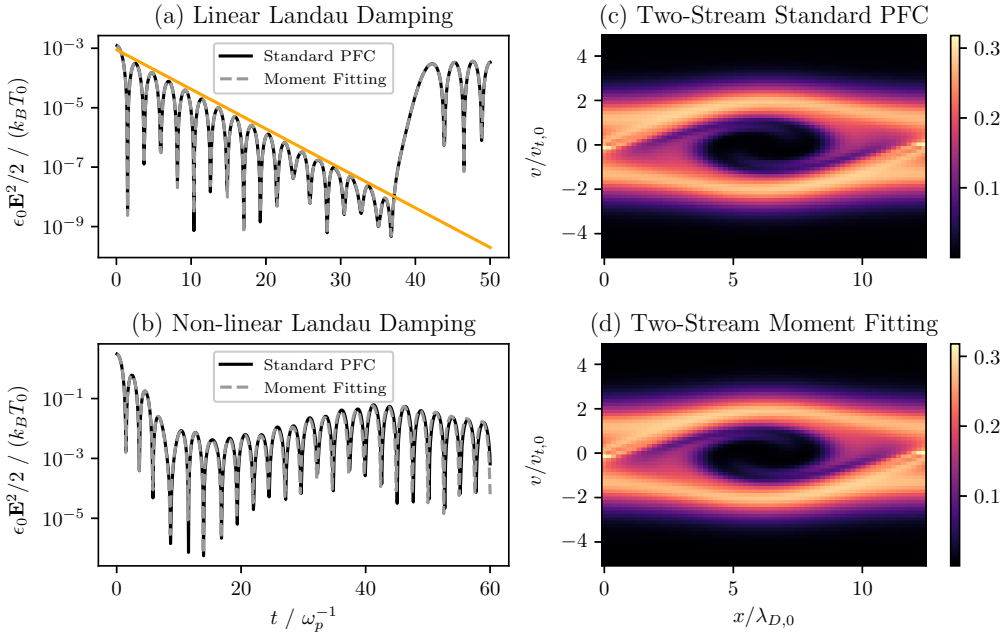


Figure 1: Comparison of the standard PFC and the moment fitting Vlasov solvers. (a) Electric energy next to the analytical damping rate (orange line) in linear Landau damping, (b) electric energy in non-linear Landau damping, (c) and (d) distribution function f_e obtained from the two methods in a two-stream instability setup at $t = 30\,\omega_{p,0}^{-1}$.

The discussed setups focus on electron effects and are purely electrostatic. Therefore, we use a Poisson solver to calculate the electric field and choose the following normalization: Time in inverse electron plasma frequency $\omega_{p,0}^{-1}$, length in electron Debye length $\lambda_{D,0}$, velocity in electron thermal velocity $v_{t,0}$, mass in electron mass m_e, temperature in initial electron temperature T_0 and finally $\epsilon_0 = 1$. The initial condition for the Landau damping setup is $f_{e,0}(x,v) = \frac{1}{\sqrt{2\pi}}\,\exp(-v^2/2)\,(1+\alpha\cos(kx))$ with $k = 0.5\,\lambda_{D,0}^{-1}$ and a static and spatially uniform neutralizing ion background. The one-dimensional domain has an extent of $-2\pi\,\lambda_{D,0}$ to $2\pi\,\lambda_{D,0}$ and the velocity space of $-v_{\max}$ to $v_{\max}$. In the linear Landau damping case it is $v_{\max} = 4.5\,v_{t,0}$

and $\alpha = 0.01$ with a resolution of 32×32 cells, whereas in the non-linear case it is $v_{\max} = 6\, v_{t,0}$ and $\alpha = 0.5$ with a resolution of 32×64 cells. The two-stream instability initial condition is $f_{e,0}(x, v) = \frac{1}{\sqrt{2\pi}}\, v^2\, \exp(-v^2/2)\, (1 + \alpha \cos(kx))$ with $v_{\max} = 5\, v_{t,0}$, $\alpha = 0.01$ and a domain from 0 to $4\pi\, \lambda_{D,0}$. The resolution is 64×64 cells.

Fig. 1(a) shows the damping of electric wave energy obtained from standard PFC (black) and moment fitting (gray dotted) simulations of linear Landau damping together with the analytic damping rate (orange). The results are mostly identical and in both cases the damping rate is $\gamma = 0.153\, \omega_{p,0}^{-1}$ (analytic: $\gamma = 0.1533\, \omega_{p,0}^{-1}$) and the oscillation frequency is $\omega = 1.41\, \omega_{p,0}$ (analytic: $\omega = 1.416\, \omega_{p,0}$). Non-linear Landau damping is also equally well represented by both methods as shown in Fig. 1(b). The same results can be found in Filbet et al. [2001]. In Fig. 1(c) and 1(d) it is shown that the distribution functions obtained from the standard PFC scheme and the moment fitting scheme also match in the highly non-Maxwellian case of a two-stream instability.

3.2 Orszag-Tang Turbulence

A plasma turbulence setup is well-suited for testing the moment fitting Vlasov solver (and also the gradient fluid solver) because of the broad range of plasma phenomena that are relevant for the dissipation of energy like multiple types of waves, magnetic reconnection and Landau damping. The Orszag-Tang turbulence setup we use has periodic boundary conditions and thus is also a good setup to check the solvers' conservation properties. As we will show, the moment fitting Vlasov solver yields results that agree with those from a published fully kinetic particle-in-cell (PIC) simulation.

The initial conditions are taken from Grošelj et al. [2017] (parameters A1). The magnetic field is $B_x = -\delta_B \sin(2\pi y/L)$, $B_y = \delta_B \sin(4\pi x/L)$ and $B_z = 1B_0$ and the velocities are $u_{x,s} = -\delta_u \sin(2\pi y/L)$, $u_{y,s} = \delta_u \sin(2\pi x/L)$, $u_{z,i} = 0$ and $u_{z,e} = -\frac{2\pi}{L}\delta_B \mu_0 (2\cos(4\pi x/L) + \cos(2\pi y/L))$. Here, the magnitude of the perturbation is given by $\delta_u = 0.2 v_{A,0}$ and $\delta_B = 0.2 B_0$. In z-direction a current results from Faraday's law which is accounted for by the electron velocity. Ideal MHD Ohm's law yields for the electric field $E_x = -\delta_u B_0 \sin(2\pi x/L)$, $E_y = -\delta_u B_0 \sin(2\pi y/L)$ and $E_z = 0$. The initial density is uniform $n_s = n_0$ apart from a small perturbation added to the electron density to satisfy Gauss's law. Temperatures are defined via $T_i/T_e = 1$ and $\beta_i = 2\mu_0 n_0 k_B T_i / B_0^2 = 0.1$. Ion-electron mass ratio is set to $m_i/m_e = 100$ and speed of light to $c = 18.174\, v_{A,0}$. The spatial resolution is 512^2 in the Vlasov simulations (two cells per electron inertial length) and 2048^2 in the fluid simulation. The velocity space in the Vlasov case goes from $-14\, v_{A,0}$ to $14\, v_{A,0}$ for the electrons and from $-1.5\, v_{A,0}$ to $1.5\, v_{A,0}$ for the ions, each resolved by 34^3 cells.

Three numerical models are compared in Fig. 2: The moment fitting Vlasov solver, the standard PFC Vlasov solver and the fluid solver with gradient heat flux closure (Eq. (5)). In the upper row the distribution of energy over time is shown whereas the lower row gives an impression of the current density's spatial structure in out-of-plane direction. Looking at the current density, it is immediately evident that there is good agreement between the moment fitting Vlasov model and the gradient fluid model while the standard Vlasov solver stands out. The reason can be identified from the energy plots which show magnetic energy $\int \mathrm{d}^3\mathrm{x}\ \mathbf{B}^2/(2\mu_0)$, ion kinetic energy $\int \mathrm{d}^3\mathrm{x}\ m_i n_i \mathbf{u}_i^2/2$ and species thermal energies $\int \mathrm{d}^3\mathrm{x}\ (N/2) n_s k_B T_s$ where N is the dimensionality of velocity space. Total energy $\mathcal{E} = \int \mathrm{d}^3\mathrm{x}\ \sum_s (m_s n_s \mathbf{u}_s^2/2 + n_s k_B T_s) + \mathbf{B}^2/(2\mu_0) + \epsilon_0 \mathbf{E}^2/2$ is conserved in the Vlasov-Maxwell system with periodic boundary conditions. However, the standard Vlasov solver suffers from substantial numerical heating so that electron thermal energy increases to four times the initial value. In consequence, total energy reaches 1.5 times the initial value by the end of the simulation. The moment fitting Vlasov solver on the other hand conserves energy well with an error smaller than $5 \cdot 10^{-5}\, \mathcal{E}(t = 0)$ as shown in Fig. 3.

In both the moment fitting Vlasov model and the fluid model ion kinetic energy is first converted into magnetic energy. After $t = 40\, \Omega_{i,0}$ the magnetic energy is partly converted back to ion kinetic energy through magnetic reconnection. Over time magnetic and kinetic energy decrease in favor of thermal energy as expected in a turbulent plasma. In gyrokinetic turbulence Kawazura et al. [2019] found that when the magnetic energy is larger than the thermal energy, electrons are typically more strongly heated than ions. This is also the case in the kinetic moment fitting simulation here, in agreement with the PIC and gyrokinetic simulations from Grošelj et al. [2017]. Generally, the evolution of energy distribution is in excellent agreement with Grošelj et al. [2017] (note the different normalization). However, the fluid model does not correctly predict the ratio of electron

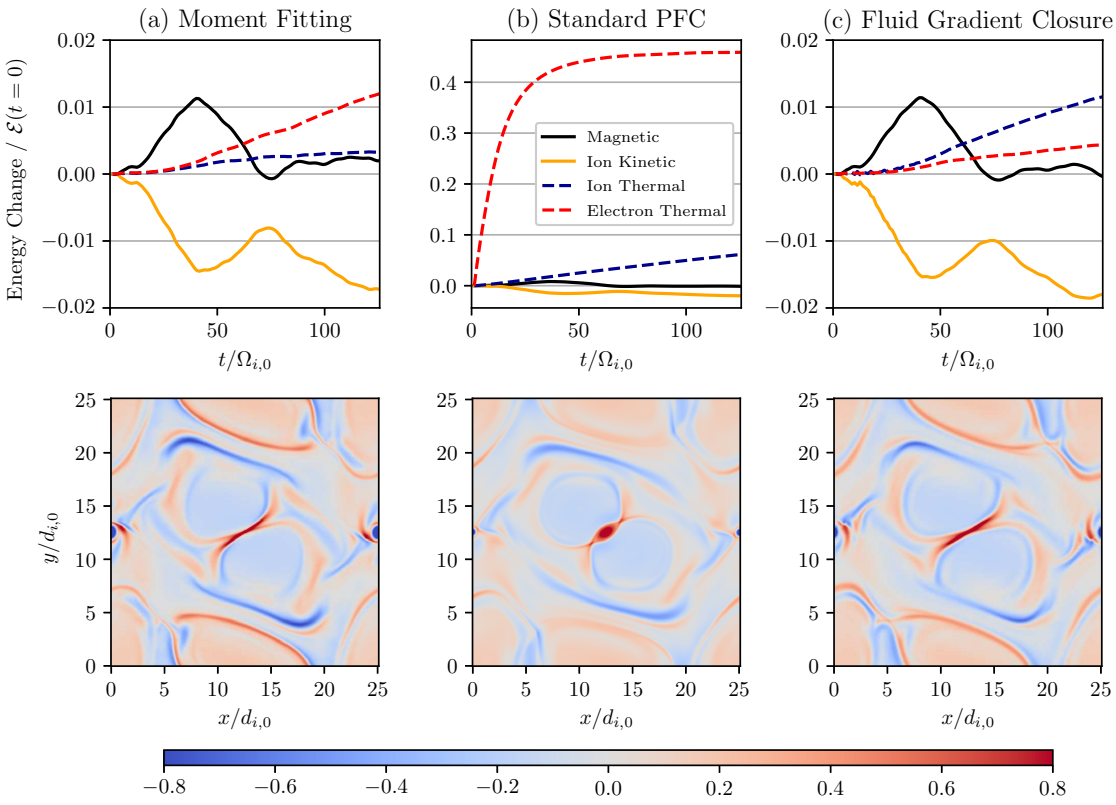


Figure 2: The deviation of magnetic energy, ion kinetic energy, ion thermal energy and electron thermal energy from the initial values and the out-of-plane current density $j_z/(q_i n_0 v_{A,0})$ at $t = 62.83\,\Omega_{i,0}$ in Orszag-Tang turbulence. Shown for (a) the moment fitting Vlasov solver, (b) the standard PFC Vlasov solver and (c) the gradient closure fluid solver.

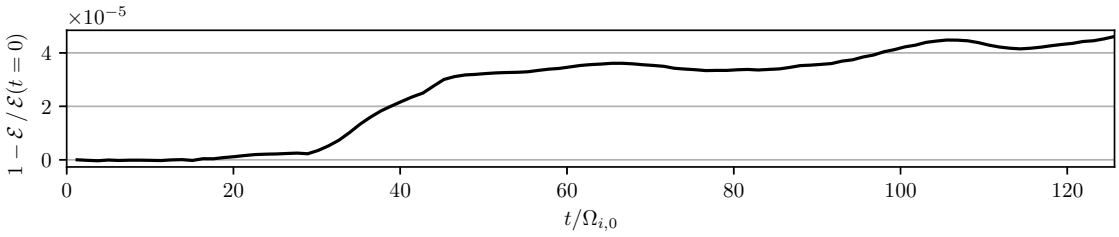


Figure 3: Error in total energy conservation over time in the moment fitting Vlasov simulation of Orszag-Tang turbulence.

and ion thermalization. This could be improved by fine-tuning the characteristic spatial frequencies in the gradient closure expression (Eq. (5)), which have direct influence on the magnitude of the heat flux and therefore on dissipation and heating.

The current density structure of both the moment fitting kinetic model and the fluid model (Fig. 2(d),(f)) matches that of the PIC simulation in Grošelj et al. [2017]. In the center of the domain a current sheet has formed where magnetic field lines reconnect. The numerically heated plasma in the standard Vlasov model features increased dissipation so that in this case a magnetic island forms within the current sheet. The heating is less problematic for lower mass ratios like $m_i/m_e = 25$ because of the smaller extent of electron velocity space and the resulting smaller cell sizes. In that case, however, the ion and electron scales are not separated well leading to over- or underestimation of electron effects with influence on the turbulence development. The geometry at the shown time has another interesting detail which is the magnetic o-point at the left and right domain borders at $y = L_y/2$. The o-point is present in fully kinetic simulations and is correctly caught by the gradient fluid model. In contrast, the – compared to multi-fluid – much more expensive gyrokinetic and hybrid kinetic models do not catch this detail (see Fig. 1 of Grošelj et al. [2017]).

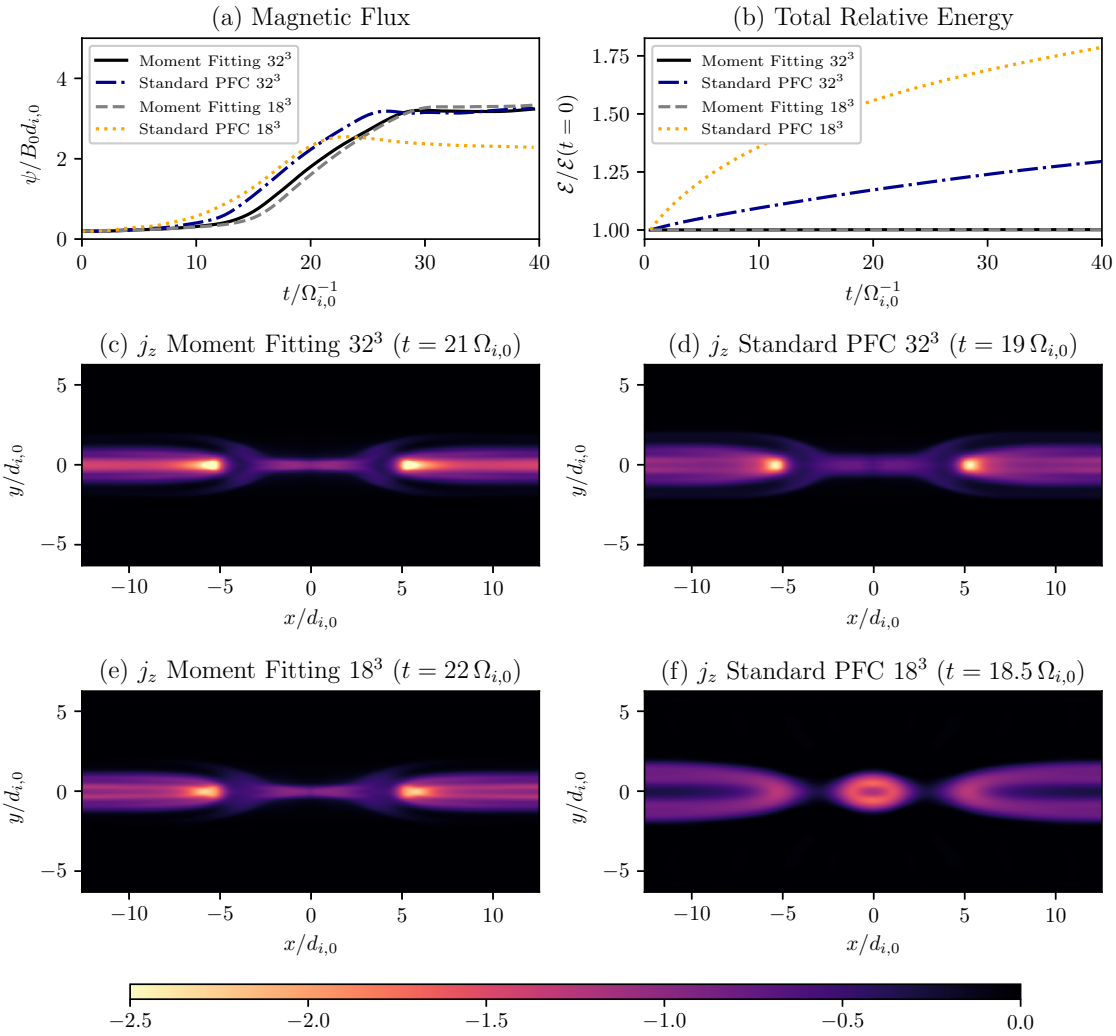


Figure 4: Comparison of the moment fitting and the standard PFC Vlasov solvers at velocity space resolutions of 32^3 and 18^3. The out-of-plane current density $j_z/(q_i n_0 v_{A,0})$ is shown when the magnetic flux is $\psi = 2\,B_0 d_{i,0}$.

3.3 GEM Reconnection

One central advantage of the moment fitting Vlasov method is that the numerical necessity for high velocity resolutions is relaxed. To demonstrate this, we employ the GEM reconnection problem [Birn et al., 2001] that has been studied extensively by many authors and compare moment fitting Vlasov simulations at low velocity space resolutions with higher-resolved moment fitting as well as standard PFC simulations.

The initial configuration is given by a Harris equilibrium with density $n_s = n_0\,\mathrm{sech}^2(y/\lambda) + n_b$ and magnetic field $B_x = \tanh(y/\lambda)B_0 + \delta B_x$, $B_y = \delta B_y$. The background density is $n_b = 0.2\,n_0$ and the half-width of the current sheet is $\lambda = 0.5\,d_{i,0}$. The temperature is uniform and defined by $n_0 k_B(T_e + T_i) = B_0^2/(2\mu_0)$, $T_i/T_e = 5$. A perturbation of the magnetic field is added to initiate the reconnection process which is given by $\delta B_x = -\psi_0 \pi/L_y \cos(2\pi x/L_x)\sin(\pi y/L_y)$, $\delta B_y = \psi_0 2\pi/L_x \sin(2\pi x/L_x)\cos(\pi y/L_y)$ with $\psi_0 = 0.1 B_0 d_{i,0}$. The magnetic field gradients are associated with a current density which is distributed among electrons and ions according to $u_{z,i}/u_{z,e} = T_i/T_e$. All particles contribute to the current density without discrimination between background and sheet particles. The reduced ion to electron mass ratio and speed of light are $m_i/m_e = 25$ and $c = 20\,v_{A,0}$, respectively. The simulated domain is of size $L_x \times L_y = (8\pi \times 4\pi)\,d_{i,0}$, here resolved by 512×256 cells. It is periodic in x-direction, has conducting walls for fields and reflecting walls for particles in y-direction and is translationally symmetric in z-direction. Electron velocity space ranges from $-12.5\,v_{A,0}$ to $12.5\,v_{A,0}$ and ion velocity space from $-5\,v_{A,0}$ to $5\,v_{A,0}$.

In Fig. 4(a) the development of the reconnected flux is compared between the moment fitting and the standard PFC Vlasov solver at velocity space resolutions of 32^3 and 18^3. Both high-resolution runs and the low-resolution moment fitting run feature a similar slope and saturation, indicating identical reconnection physics in the three simulations. Onset of reconnection is slightly earlier when the standard Vlasov solver is used because of the higher electron temperature caused by numerical heating. The effect of large velocity space cell sizes is clearly evident in Fig. 4(b). While the well-resolved standard Vlasov run has an energy conservation error of 25% at the end of the simulation, the run with lower v-space resolution violates energy conservation by even 75%, accompanied by an incorrect representation of the reconnection process. While non-positive energy conserving Vlasov schemes do not have this issue, they suffer from numerical oscillations which at such low resolutions typically impair the reconnection significantly and often render the simulation unstable. On the contrary, the moment fitting Vlasov model conserves total energy for both resolutions without numerical oscillations. Of course velocity space resolution cannot be arbitrarily low also for the moment fitting method: The relevant physical features in the distribution function must still be appropriately represented by the discretization and the numerical errors from the advection scheme and the discretized integration to obtain heat flux must be sufficiently small.

The out-of-plane current density profiles shown in Fig. 4(c)-(f) agree as far as the moment fitting simulations and the high-resolution standard PFC simulation are concerned. In contrast, the low-resolution standard PFC simulation (Fig. 4(f)) shows incorrect results. Similar to the reconnection layer in the turbulence simulation (Fig. 2(b)) a magnetic island forms due to the high temperature. At the same low resolution of 18^3, the moment fitting Vlasov method yields good results that can even be considered more accurate than those obtained from the standard method at 32^3 as the current sheet is thinner and less dissipated.

4 MMS Reconnection Events

4.1 Magnetotail

On 11th July 2017 at 22:34 UT a reconnection event in the Earth's magnetotail was measured by the MMS spacecraft as described in detail by Torbert et al. [2018]. In the two papers by Nakamura et al. [2018] and Genestreti et al. [2018] physical parameters were extracted from the MMS measurements as initial conditions for a fully kinetic PIC simulation and excellent agreement between the simulation results and the measurement data was found as well as accurate estimations of the reconnection rate in this magnetotail event. Here, we perform a simulation with the same initial conditions as in Nakamura et al. [2018] using the moment fitting Vlasov solver to confirm their simulation results and to verify the Vlasov solver with data from MMS measurements. The absence of noise also allows us to analyze heat flux in our simulation and thus in the modelled reconnection event.

The initial spatial profiles of density and magnetic field again follow from the Harris equilibrium: $n_s = n_0 \operatorname{sech}^2(y/\lambda) + n_b$, $B_x = \tanh(y/\lambda) B_0 + \delta B_x$, $B_y = \delta B_y$ and $B_z = -B_g$. The plasma parameters are $n_b = n_0/3$, $\lambda = 0.6\, d_{i,0}$ and guide field $B_g = 0.03\, B_0$. There is now a discrimination between sheet particles (those with density $n_0 \operatorname{sech}^2(y/\lambda)$) and background particles (those with density n_b). The sheet particles get temperatures defined by $n_0 k_B (T_{0,e} + T_{0,i}) = B_0^2/(2\mu_0)$, $T_{0,i}/T_{0,e} = 3$ and are responsible for the total current density. The background particles are initially static and have temperatures $T_{bg,s} = T_{0,s}/3$. Maxwellian distributions are calculated for sheet and background particles and then added up. Reconnection is initiated by a small Gaussian perturbation $\delta B_x = -\xi\,(2y/\lambda)\, \exp\left(-(x/(a\lambda))^2\right) \exp\left(-(y/\lambda)^2\right)$ and $\delta B_y = \xi\,(2x/(a\lambda))\, \exp\left(-(x/(a\lambda))^2\right) \exp\left(-(y/\lambda)^2\right)$ where $a = L_x/L_y$ and $\xi = 0.01$. To break the symmetry we also add random noise of magnitude $10^{-6}\, B_0$ to B_x. The domain goes from $-L_x/2$ to $L_x/2$ in x-direction and $-L_y/2$ to $L_y/2$ in y-direction and with $L_x = 120\, d_{i,0}$ and $L_y = 40\, d_{i,0}$. Electron velocity space ranges from $-20\, v_{A,0}$ to $20\, v_{A,0}$ and ion velocity space from $-5\, v_{A,0}$ to $5\, v_{A,0}$. We set the ion-electron mass ratio to $m_i/m_e = 100$ and the speed of light to $c = 30\, v_{A,0}$. The resolution is $1536 \times 512 \times 36^3$ cells. The simulation quantities transfer to SI units using $n_0 = 0.09\,\mathrm{cm}^{-3}$ and $B_0 = 12\,\mathrm{nT}$ [Nakamura et al., 2018] so that $d_{i,0} = 759.0\,\mathrm{km/s}$, $d_{e,0} = 17.71\,\mathrm{km/s}$, $v_{A,0} = 872.5\,\mathrm{km/s}$, $v_{A,e,0} = 37\,386\,\mathrm{km/s}$ and $E_0 = v_{A,0} B_0 = 10.47\,\mathrm{mV/m}$.

In Fig. 5 the MMS3 measurements are shown next to the simulation data along a virtual path through the electron diffusion region, visualized by the white line in Fig. 5c. Cell aver-

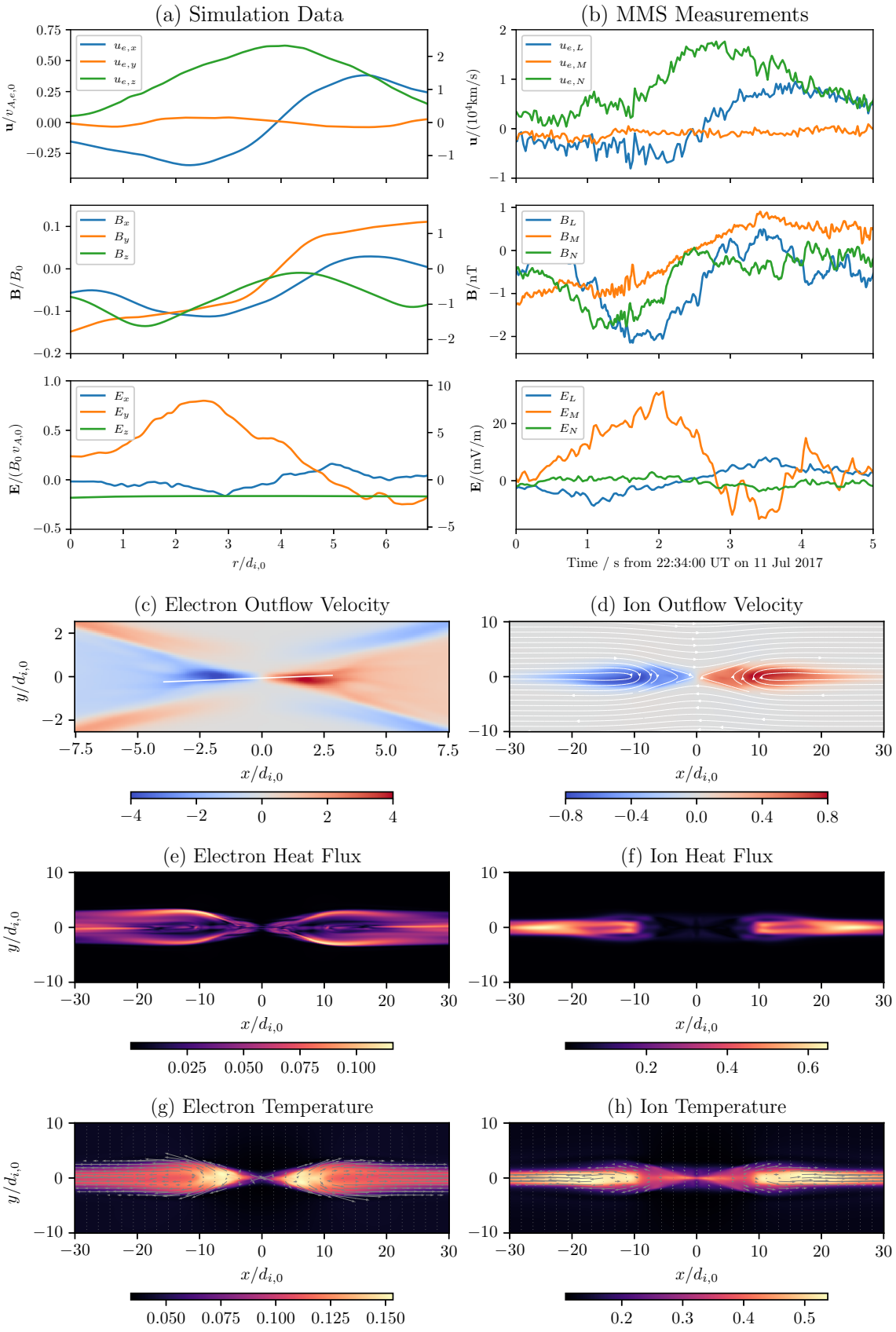


Figure 5: (a) Electron velocity, magnetic field and electric field along a virtual path in the magnetotail reconnection simulation at $t = 75\,\Omega_i$ and (b) as measured by MMS and (c-h) simulation state at $t = 75\,\Omega_i$. (c) $u_{x,e}/v_{A,0}$ and the virtual path, (d) $u_{x,i}/v_{A,0}$ alongside the magnetic field lines, (e) electron heat flux scalar $|\mathbf{q}_e|/(m_i n_0 v_{A,0}^3)$, (f) ion heat flux scalar $|\mathbf{q}_i|/(m_i n_0 v_{A,0}^3)$, (g) $T_e/(m_i v_{A,0}^2/k_B)$ and direction of $\mathbf{q}_e$ as arrows, (h) $T_i/(m_i v_{A,0}^2/k_B)$ and direction of $\mathbf{q}_i$ as arrows.

ages in the simulation are interpolated to the path using a bivariate spline interpolator. The simulation frame is the plasma's rest frame and the virtual path models the movement of the plasma away from Earth through the MMS spacecraft. The measurements are transferred from GSM coordinates to the simulation coordinate system according to $L = [0.9482, -0.2551, -0.1893]$, $M = [0.2651, 0.3074, 0.9139]$, $N = [-0.1749, -0.9168, 0.3591]$, which is the coordinate system obtained by Genestreti et al. [2018] adapted to our simulation axes. We use publicly available data from the dual electron spectrometers [Pollock et al., 2016], the fluxgate magnetometer [Russell et al., 2016] and the electric field double probe [Ergun et al., 2016, Lindqvist et al., 2016]. There is excellent agreement between simulation and measurements both qualitatively and quantitatively. Differences in magnitude, especially of the electric field, can be attributed to the artificially reduced ion-electron mass ratio in the simulation. The simulation also agrees very well with the much better resolved and computationally more expensive PIC simulation in Nakamura et al. [2018] concerning both reconnection rate and spatial structures. Of course their simulation is highly accurate (the resolution is better, and m_i/m_e is higher) and more computational resources have been invested than in the Vlasov simulation presented here. Nevertheless, it should also be taken into account that we restricted our virtual path to a straight line while they allowed fluctuations around a straight path which gives more freedom to match the measurement data. The Vlasov approach has advantages in the representation of the electric field which is free of noise. This clearly shows in the good agreement between simulated and measured electric field. The difference between the measurement of E_N and the simulation E_z is due to difficulties in measuring the offset of the out-of-plane electric field [Genestreti et al., 2018].

Panels (c) and (d) of Fig. 5 show zoomed-in views of the electron and ion outflow velocities, respectively. Electron outflow saturates at $\sim 0.4\, v_{A,e,0}$ and ion outflow has peak velocities of $\sim 1.1\, v_{A,0}$ at later times. The magnetic field lines shown in panel (d) have clearly reconnected at the time. Since there is no discrete particle noise in the Vlasov simulation, an accurate analysis of heat flux in the simulation is possible. We plotted the magnitude of the electron heat flux vector $|\mathbf{q}_e|$ in Fig. 5(e) and its direction together with electron temperature T_e in Fig. 5(g). There are peaks in heat flux at the separatrix borders which correspond to peaks in the electric field. Thus, electron heat flux is dominated by energy transfer from the electric field to the particles, one important mechanism being electron Landau damping. Comparing the locality of heat flux with the temperature profile, it is evident that heat flux is often located where temperature gradients are strong as for example at the separatrix border. However, the heat flux is not necessarily along the temperature gradients because fluctuations that are subject to Landau damping are primarily in direction of the magnetic field which is reflected in the direction of the heat flux. This also shows both the good potential and the deficits of the temperature gradient closure (5) that we used for modelling Landau damping within the ten-moment multifluid simulations of plasma turbulence in Sec. 3.2. The gradient closure captures the location of heat flux at the temperature gradients, but the magnetic field should be taken into account to better capture the direction of the heat flux.

In Fig. 5(f) and (h), heat flux and temperature are shown for the ions. Ion heat flux differs significantly from electron heat flux both concerning location and mechanism. While there is some heat flux at the separatrix boundaries, much more is present in the outflow with a peak where the magnetic field is the strongest – in Fig. 5 visible at $x \approx \pm 10\, d_{i,0}$. There, heat flux is generated through remagnetization of the outflowing ions which start to gyrate and thus are more susceptible to wave-particle interactions. In consequence part of their kinetic energy is converted into thermal energy. Ion heating due to remagnetization in the ouflow has also been measured in laboratory reconnection [Yamada et al., 2014]. Unexpectedly, there is a second place of strong heat flux further downstream (starting from $x \approx \pm 20\, d_{i,0}$) which is caused by fluctuations in x-direction, i.e. dominated by the Q_{xxx} component of the heat flux tensor. To weaker extent it is also present in the electrons. This second heat flux peak is located at the head of the outflow where the outflow particles meet current sheet and background particles that have not been accelerated in x-direction. One explanation of the heat flux is a possibly increased wave activity in this region due to the outflow, accompanied by energy transfer through wave-particle interactions. Microinstabilities related to the different velocity distributions of the outflow particles compared to the sheet and background particles might also cause heat flux.

4.2 Foreshock

In Liu et al. [2020] two reconnection events measured by MMS in the Earth's foreshock are reported and modelled with PIC simulations. The event with a strong guide field that we want to

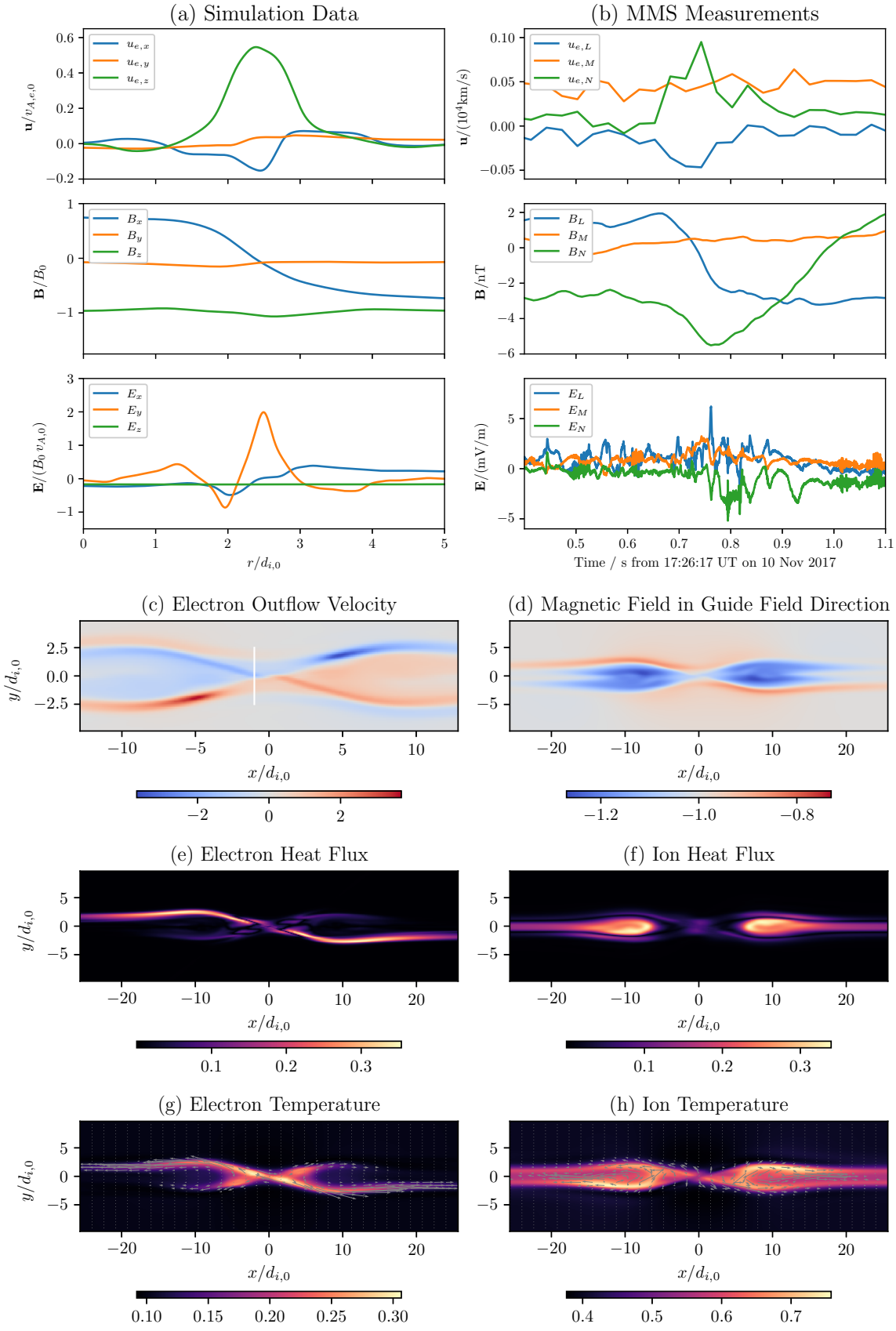


Figure 6: (a) Electron velocity, magnetic field and electric field along a virtual path in the foreshock reconnection simulation at $t = 30\,\Omega_i$ and (b) as measured by MMS and (c-h) simulation state at $t = 30\,\Omega_i$. (c) $u_{x,e}/v_{A,0}$ and the virtual path, (d) B_z/B_0, (e) electron heat flux scalar $|\mathbf{q}_e|/(m_i n_0 v_{A,0}^3)$, (f) ion heat flux scalar $|\mathbf{q}_i|/(m_i n_0 v_{A,0}^3)$, (g) $T_e/(m_i v_{A,0}^2/k_B)$ and direction of $\mathbf{q}_e$ as arrows, (h) $T_i/(m_i v_{A,0}^2/k_B)$ and direction of $\mathbf{q}_i$ as arrows.

discuss took place on 10th November 2017 at 17:26:17 UT. We perform a Vlasov simulation and compare it to measurements and PIC results. The initial conditions are as described in Sec. 4.1 but with the plasma parameters that were chosen by Liu et al. [2020]: The guide field is now $B_g = 1B_0$, the background density is $n_{bg} = 0.2\,n_0$, temperature ratio is $T_{0,i}/T_{0,i} = T_{bg,i}/T_{bg,i} = 4$, initial current sheet half-width is $\lambda = 0.5\,d_{i,0}$, speed of light is $c = 20\,v_{A,0}$ and the domain is of size $L_x = 102.4\,d_{i,0}$, $L_y = 25.6\,d_{i,0}$. We use a resolution of $1152 \times 288 \times 36^3$ cells and $\xi = 0.025$ as the initial perturbation's magnitude.

A comparison between the simulation data interpolated along a virtual path and the publicly available MMS1 data is shown in Fig. 6. The measurements are transferred from GSE coordinates to the simulation coordinate system as given by Liu et al. [2020], adapted to our simulation axes: $L = [0.58, 0.24, 0.78]$, $M = [-0.50, 0.85, 0.11]$, $N = [-0.64, -0.45, 0.62)]$. There is good qualitative agreement between simulation and MMS data for example in the out-of-plane electron velocity $u_{z,e}$ caused by the reconnecting magnetic field and in the electron outflow velocity $u_{x,e}$. In both simulation and measurements there is an oppositely directed B_x above and below the x-line current sheet. The guide field B_z has in both cases the same quantitative relation to the background field B_x. In the measured event the guide field rises strongly after passing a local minimum which may be caused by turbulence in the foreshock reconnection and is not seen in the two-dimensional simulation. Also, the electric fields only fit very roughly. Quantitatively the measured electric field and the electron velocities are rather low compared to the simulation. Quantitative agreement between model and measurements cannot be expected – a more precise estimate of the initial plasma parameters and possibly a three-dimensional simulation to account for instabilities and turbulence would be necessary. Nevertheless, the qualitative agreement suggests that the measured current sheet is indeed due to magnetic reconnection.

The electron outflow velocity $u_{x,e}$ is shown in Fig. 6(c). It differs notably from the weak guide field case (Fig. 5(c)) and has maxima along the separatrix boundaries with low B_z on the sides where E_x is in outflow direction. The outflow velocity is reduced by the guide field, peaks at $\sim 0.37\,v_{A,e,0}$ and later goes back down to $\sim 0.22\,v_{A,e,0}$, much lower than when the guide field is weak. On the contrary, ion outflow velocity becomes larger (here $\sim 1.5\,v_{A,0}$ later in the simulation) when the guide field is strong, as has been suggested by Haggerty et al. [2018]. For a direct comparison of the spatial structure with the PIC simulation in Liu et al. [2020] we have plotted the out-of-plane magnetic field in Fig. 6(d). There is good agreement between the two methods, their PIC results are overall very similar to the continuum Vlasov results here.

Electron heat flux (Fig. 6(e)) in this strong guide field scenario is even more localized at the separatrix border than in the weak guide field simulation. It is again related to peaks of the electric field which now has a stronger preference for one side of the separatrix border due to the stronger guide field. Electron temperature (panel (g)) has its maximum along the x-line current sheet and is less spread out compared to the weak guide field case because heating is reduced perpendicular to the guide field. Ion heat flux (panel (f)) is dominated by the Q_{zzz} component of the heat flux tensor. It has a peak next to the maximum of $|B_y|$ at $(x, y) \approx \pm(7, 0)\,d_{i,0}$ and another peak where $|B_x|$ and $|B_z|$ are both large at $(x, y) \approx \pm(10, 1)\,d_{i,0}$. That means even when there is a strong guide field, a rapid increase in magnetic field strength leads to a transfer of the ion kinetic energy to thermal energy. However, it is evident in the lower magnitude of the heat flux compared to the weak guide field case that the particles are already magnetized before entering the area where the magnetic field strength increases. The in-plane direction of the heat flux vector shown in Fig. 6(h) varies heavily near the magnetic o-line due to the fast changing direction of the magnetic field at this place. Ion temperature (Fig. 6(h)) is the highest near the separatrix border which may be associated with the transport of heated ions into this region along with the outflow.

5 Conclusions

Traditional continuum Vlasov schemes have the reputation of being computationally expensive which is due to the numerical necessity of high velocity space resolutions. Unlike in PIC simulations, a coarse representation of velocity space may lead to non-conservation of energy or numerical oscillations. Consequently, continuum Vlasov simulations were primarily applied to small-scale or two-dimensional problems, or electrons were treated non-kinetically. To address this issue, we developed a new dual Vlasov solver which uses a standard positivity-preserving Vlasov scheme to update the distribution function, and an energy conserving partial differential equation solver to update velocities and temperatures. By means of moment fitting, the schemes can work together

as a positivity-preserving and energy-conserving Vlasov solver that has good stability properties and deals well with coarse velocity space resolutions.

The new method enables us to address large-scale non-linear problems with continuum Vlasov simulations. We performed simulations of reconnection events measured by the MMS probe and obtained excellent agreement with measurements. In the simulated reconnection events in the Earth's magnetosphere electron heat flux is dominated by energy transfer from the electric field to the electrons while ion heat flux is dominated by transfer of ion kinetic energy to thermal energy via remagnetization. A Vlasov solver like the one presented in this paper can compete with PIC solvers concerning computational cost. The continuum Vlasov simulations presented in this paper agree well with published PIC simulations, validating both methods. The continuum method and the PIC method have their respective strenghts and it is valuable to have different options at hand for fully kinetic modelling of large-scale plasmas.

The next step will be spatial coupling of the Vlasov model to multi-fluid and MHD models in order to reach global scales. The continuum Vlasov model is well-suited for smooth spatial coupling since the noise-free distribution function is available [Rieke et al., 2015, Lautenbach and Grauer, 2018]. Using an energy conserving Vlasov solver eases the coupling because temperature gradients at the model interfaces due to numerical heating [Rieke et al., 2015] are avoided. Ideally a plasma is represented by a hierarchy of models from fully-kinetic over hybrid-kinetic to multi-fluid and MHD models depending on the plasma effects that need to be captured in the respective regions. In this hierarchy ten-moment multifluid models can be efficiently used. In many cases they can approximate kinetic plasmas well as we have shown in the present paper at the example of a plasma turbulence simulation. The ten-moment multifluid model may be used either on its own or as an accurate electron model in hybrid fluid-kinetic simulations.

There is potential to further improve the moment fitting Vlasov solver in the future. The partial differential equation solver may be extended to not only conserve energy but also conserve momentum (similar to Amano and Kirk [2013], Balsara et al. [2016]) so that the resulting dual Vlasov solver will then preserve positivity and conserve charge, energy and additionally momentum. The moment fitting method is also a candidate to make low-rank Vlasov simulations [Kormann, 2015] conservative. Using low-rank decomposition and compression of the distribution function, much higher velocity space resolutions (larger than 128^3 cells) become possible.

Acknowledgments

We thank Michael Abolnikov for interesting discussions and first tests of the moment fitting method. We gratefully acknowledge the Gauss Centre for Supercomputing e.V. (www.gauss-centre.eu) for funding this project by providing computing time through the John von Neumann Institute for Computing (NIC) on the GCS Supercomputer JUWELS at Jülich Supercomputing Centre (JSC). Computations were conducted on JUWELS-booster [Jülich Supercomputing Centre, 2019] and on the DaVinci cluster at TP1 Plasma Research Department. F.A. was supported by the Helmholtz Association (VH-NG-1239). We thank the MMS team for the measurement data available at the MMS Science Data Center (https://lasp.colorado.edu/mms/sdc/). We used the pySPEDAS software (https://github.com/spedas/pyspedas) and the SpacePy software (https://spacepy.github.io/) for data processing; thanks to the respective developers.

References

F. Allmann-Rahn, T. Trost, and R. Grauer. Temperature gradient driven heat flux closure in fluid simulations of collisionless reconnection. *Journal of Plasma Physics*, 84(3):905840307, 2018. doi: 10.1017/S002237781800048X.

F. Allmann-Rahn, S. Lautenbach, R. Grauer, and R. D. Sydora. Fluid simulations of three-dimensional reconnection that capture the lower-hybrid drift instability. *Journal of Plasma Physics*, 87(1):905870115, 2021. doi: 10.1017/S0022377820001683.

Takanobu Amano and John G. Kirk. The role of superluminal electromagnetic waves in pulsar wind termination shocks. *ApJ*, 770(1):18, 2013. doi: 10.1088/0004-637X/770/1/18.

Dinshaw S. Balsara, Takanobu Amano, Sudip Garain, and Jinho Kim. A high-order relativistic two-fluid electrodynamic scheme with consistent reconstruction of electromagnetic fields and a multidimensional Riemann solver for electromagnetism. *Journal of Computational Physics*, 318: 169–200, 2016. ISSN 0021-9991. doi: 10.1016/j.jcp.2016.05.006.

J. Birn, J. F. Drake, M. A. Shay, B. N. Rogers, R. E. Denton, M. Hesse, M. Kuznetsova, Z. W. Ma, A. Bhattacharjee, A. Otto, and P. L. Pritchett. Geospace environmental modeling (GEM) magnetic reconnection challenge. *Journal of Geophysical Research: Space Physics*, 106(A3): 3715–3719, 2001. ISSN 2156-2202. doi: 10.1029/1999JA900449.

J. L. Burch, T. E. Moore, R. B. Torbert, and B. L. Giles. Magnetospheric multiscale overview and science objectives. *Space Science Reviews*, 199:5–21, 2016. doi: 10.1007/s11214-015-0164-9.

C.Z Cheng and Georg Knorr. The integration of the Vlasov equation in configuration space. *Journal of Computational Physics*, 22(3):330–351, 1976. ISSN 0021-9991. doi: 10.1016/0021-9991(76)90053-X.

R. E. Ergun, S. Tucker, J. Westfall, K. A. Goodrich, D. M. Malaspina, D. Summers, J. Wallace, M. Karlsson, J. Mack, N. Brennan, B. Pyke, P. Withnell, R. Torbert, J. Macri, D. Rau, I. Dors, J. Needell, P.-A. Lindqvist, G. Olsson, and C. M. Cully. The axial double probe and fields signal processing for the MMS mission. *Space Science Reviews*, 199(1):167–188, 2016. ISSN 1572-9672. doi: 10.1007/s11214-014-0115-x.

Francis Filbet, Eric Sonnendrücker, and Pierre Bertrand. Conservative numerical schemes for the Vlasov equation. *Journal of Computational Physics*, 172(1):166 – 187, 2001. ISSN 0021-9991. doi: 10.1006/jcph.2001.6818.

K. J. Genestreti, T. K. M. Nakamura, R. Nakamura, R. E. Denton, R. B. Torbert, J. L. Burch, F. Plaschke, S. A. Fuselier, R. E. Ergun, B. L. Giles, and C. T. Russell. How accurately can we measure the reconnection rate EM for the MMS diffusion region event of 11 July 2017? *Journal of Geophysical Research: Space Physics*, 123(11):9130–9149, 2018. doi: 10.1029/2018JA025711.

Daniel Grošelj, Silvio S. Cerri, Alejandro Bañón Navarro, Christopher Willmott, Daniel Told, Nuno F. Loureiro, Francesco Califano, and Frank Jenko. Fully kinetic versus reduced-kinetic modeling of collisionless plasma turbulence. *The Astrophysical Journal*, 847(1):28, 2017. doi: 10.3847/1538-4357/aa894d.

Colby C. Haggerty, Michael A. Shay, Alexandros Chasapis, Tai D. Phan, James F. Drake, Kittipat Malakit, Paul A. Cassak, and Rungployphan Kieokaew. The reduction of magnetic reconnection outflow jets to sub-Alfvénic speeds. *Physics of Plasmas*, 25(10):102120, 2018. doi: 10.1063/1.5050530.

Ammar Hakim and James Juno. *Alias-Free, Matrix-Free, and Quadrature-Free Discontinuous Galerkin Algorithms for (Plasma) Kinetic Equations*. IEEE Press, 2020. ISBN 9781728199986.

G. W. Hammett, W. Dorland, and F. W. Perkins. Fluid models of phase mixing, Landau damping, and nonlinear gyrokinetic dynamics. *Physics of Fluids B*, 4(7):2052–2061, 1992. doi: 10.1063/1.860014.

Gregory W. Hammett and Francis W. Perkins. Fluid moment models for Landau damping with application to the ion-temperature-gradient instability. *Phys. Rev. Lett.*, 64:3019–3022, 1990. doi: 10.1103/PhysRevLett.64.3019.

Jülich Supercomputing Centre. JUWELS: Modular Tier-0/1 Supercomputer at the Jülich Supercomputing Centre. *Journal of large-scale research facilities*, 5(A135), 2019. doi: 10.17815/jlsrf-5-171.

J. Juno, A. Hakim, J. TenBarge, E. Shi, and W. Dorland. Discontinuous Galerkin algorithms for fully kinetic plasmas. *Journal of Computational Physics*, 353:110 – 147, 2018. ISSN 0021-9991. doi: 10.1016/j.jcp.2017.10.009.

J. Juno, M. M. Swisdak, J. M. Tenbarge, V. Skoutnev, and A. Hakim. Noise-induced magnetic field saturation in kinetic simulations. *Journal of Plasma Physics*, 86(4):175860401, 2020. doi: 10.1017/S0022377820000707.

Yohei Kawazura, Michael Barnes, and Alexander A. Schekochihin. Thermal disequilibration of ions and electrons by collisionless plasma turbulence. *Proceedings of the National Academy of Sciences*, 116(3):771–776, 2019. ISSN 0027-8424. doi: 10.1073/pnas.1812491116.

Katharina Kormann. A semi-Lagrangian Vlasov solver in tensor train format. *SIAM Journal on Scientific Computing*, 37(4):B613–B632, 2015. doi: 10.1137/140971270.

Katharina Kormann, Klaus Reuter, and Markus Rampp. A massively parallel semi-Lagrangian solver for the six-dimensional Vlasov–Poisson equation. *The International Journal of High Performance Computing Applications*, 33(5):924–947, 2019. doi: 10.1177/1094342019834644.

Alexander Kurganov and Doron Levy. A third-order semidiscrete central scheme for conservation laws and convection-diffusion equations. *SIAM Journal on Scientific Computing*, 22(4):1461–1488, 2000. doi: 10.1137/S1064827599360236.

Simon Lautenbach and Rainer Grauer. Multiphysics simulations of collisionless plasmas. *Frontiers in Physics*, 6:113, 2018. ISSN 2296-424X. doi: 10.3389/fphy.2018.00113.

P.-A. Lindqvist, G. Olsson, R. B. Torbert, B. King, M. Granoff, D. Rau, G. Needell, S. Turco, I. Dors, P. Beckman, J. Macri, C. Frost, J. Salwen, A. Eriksson, L. Åhlén, Y. V. Khotyaintsev, J. Porter, K. Lappalainen, R. E. Ergun, W. Wermeer, and S. Tucker. The spin-plane double probe electric field instrument for MMS. *Space Science Reviews*, 199(1):137–165, 2016. ISSN 1572-9672. doi: 10.1007/s11214-014-0116-9.

Hongtao Liu, Xiaofeng Cai, Giovanni Lapenta, and Yong Cao. Conservative semi-Lagrangian kinetic scheme coupled with implicit finite element field solver for multidimensional Vlasov Maxwell system. *Communications in Nonlinear Science and Numerical Simulation*, page 105941, 2021. ISSN 1007-5704. doi: 10.1016/j.cnsns.2021.105941.

Terry Z. Liu, San Lu, Drew L. Turner, Imogen Gingell, Vassilis Angelopoulos, Hui Zhang, Anton Artemyev, and James L. Burch. Magnetospheric multiscale (MMS) observations of magnetic reconnection in foreshock transients. *Journal of Geophysical Research: Space Physics*, 125(4): e2020JA027822, 2020. doi: 10.1029/2020JA027822. e2020JA027822 2020JA027822.

San Lu, Rongsheng Wang, Quanming Lu, V. Angelopoulos, R. Nakamura, A. V. Artemyev, P. L. Pritchett, T. Z. Liu, X.-J. Zhang, W. Baumjohann, W. Gonzalez, A. C. Rager, R. B. Torbert, B. L. Giles, D. J. Gershman, C. T. Russell, R. J. Strangeway, Y. Qi, R. E. Ergun, P.-A. Lindqvist, J. L. Burch, and Shui Wang. Magnetotail reconnection onset caused by electron kinetics with a strong external driver. *Nature Communications*, 11:5049, 2020. doi: 10.1038/s41467-020-18787-w.

T. K. M. Nakamura, K. J. Genestreti, Y.-H. Liu, R. Nakamura, W.-L. Teh, H. Hasegawa, W. Daughton, M. Hesse, R. B. Torbert, J. L. Burch, and B. L. Giles. Measurement of the magnetic reconnection rate in the Earth's magnetotail. *Journal of Geophysical Research: Space Physics*, 123(11):9150–9168, 2018. doi: 10.1029/2018JA025713.

W. M. Nevins, G. W. Hammett, A. M. Dimits, W. Dorland, and D. E. Shumaker. Discrete particle noise in particle-in-cell simulations of plasma microturbulence. *Physics of Plasmas*, 12(12): 122305, 2005. doi: 10.1063/1.2118729.

Jonathan Ng, A. Hakim, L. Wang, and A. Bhattacharjee. An improved ten-moment closure for reconnection and instabilities. *Physics of Plasmas*, 27(8):082106, 2020. doi: 10.1063/5.0012067.

O Pezzi, H Liang, J L Juno, P A Cassak, C L Vásconez, L Sorriso-Valvo, D Perrone, S Servidio, V Roytershteyn, J M TenBarge, and W H Matthaeus. Dissipation measures in weakly collisional plasmas. *Monthly Notices of the Royal Astronomical Society*, 505(4):4857–4873, 2021. ISSN 0035-8711. doi: 10.1093/mnras/stab1516.

Oreste Pezzi, Giulia Cozzani, Francesco Califano, Francesco Valentini, Massimiliano Guarrasi, Enrico Camporeale, Gianfranco Brunetti, Alessandro Retinò, and Pierluigi Veltri. ViDA: a Vlasov–DArwin solver for plasma physics at electron scales. *Journal of Plasma Physics*, 85(5): 905850506, 2019. doi: 10.1017/S0022377819000631.

C. Pollock, T. Moore, A. Jacques, J. Burch, U. Gliese, Y. Saito, T. Omoto, L. Avanov, A. Barrie, V. Coffey, J. Dorelli, D. Gershman, B. Giles, T. Rosnack, C. Salo, S. Yokota, M. Adrian, C. Aoustin, C. Auletti, S. Aung, V. Bigio, N. Cao, M. Chandler, D. Chornay, K. Christian, G. Clark, G. Collinson, T. Corris, A. De Los Santos, R. Devlin, T. Diaz, T. Dickerson, C. Dickson, A. Diekmann, F. Diggs, C. Duncan, A. Figueroa-Vinas, C. Firman, M. Freeman, N. Galassi, K. Garcia, G. Goodhart, D. Guererro, J. Hageman, J. Hanley, E. Hemminger, M. Holland, M. Hutchins, T. James, W. Jones, S. Kreisler, J. Kujawski, V. Lavu, J. Lobell, E. LeCompte, A. Lukemire, E. MacDonald, A. Mariano, T. Mukai, K. Narayanan, Q. Nguyan, M. Onizuka, W. Paterson, S. Persyn, B. Piepgrass, F. Cheney, A. Rager, T. Raghuram, A. Ramil, L. Reichenthal, H. Rodriguez, J. Rouzaud, A. Rucker, M. Samara, J.-A. Sauvaud, D. Schuster, M. Shappirio, K. Shelton, D. Sher, D. Smith, K. Smith, S. Smith, D. Steinfeld, R. Szymkiewicz, K. Tanimoto, J. Taylor, C. Tucker, K. Tull, A. Uhl, J. Vloet, P. Walpole, S. Weidner, D. White, G. Winkert, P.-S. Yeh, and M. Zeuch. Fast plasma investigation for magnetospheric multiscale. *Space Science Reviews*, 199(1):331–406, 2016. ISSN 1572-9672. doi: 10.1007/s11214-016-0245-4.

M. Rieke, T. Trost, and R. Grauer. Coupled Vlasov and two-fluid codes on GPUs. *Journal of Computational Physics*, 283:436 – 452, 2015. ISSN 0021-9991. doi: 10.1016/j.jcp.2014.12.016.

James A. Rossmanith and David C. Seal. A positivity-preserving high-order semi-Lagrangian discontinuous Galerkin scheme for the Vlasov–Poisson equations. *Journal of Computational Physics*, 230(16):6203–6232, 2011. ISSN 0021-9991. doi: 10.1016/j.jcp.2011.04.018.

C. T. Russell, B. J. Anderson, W. Baumjohann, K. R. Bromund, D. Dearborn, D. Fischer, G. Le, H. K. Leinweber, D. Leneman, W. Magnes, J. D. Means, M. B. Moldwin, R. Nakamura, D. Pierce, F. Plaschke, K. M. Rowe, J. A. Slavin, R. J. Strangeway, R. Torbert, C. Hagen, I. Jernej, A. Valavanoglou, and I. Richter. The magnetospheric multiscale magnetometers. *Space Science Reviews*, 199(1):189–256, 2016. ISSN 1572-9672. doi: 10.1007/s11214-014-0057-3.

H. Schmitz and R. Grauer. Kinetic Vlasov simulations of collisionless magnetic reconnection. *Physics of Plasmas*, 13(9):092309, 2006a. doi: 10.1063/1.2347101.

H. Schmitz and R. Grauer. Comparison of time splitting and backsubstitution methods for integrating Vlasov's equation with magnetic fields. *Comp. Phys. Comm.*, 175:86, 2006b.

Chi-Wang Shu and Stanley Osher. Efficient implementation of essentially non-oscillatory shock-capturing schemes. *Journal of Computational Physics*, 77(2):439 – 471, 1988. ISSN 0021-9991. doi: 10.1016/0021-9991(88)90177-5.

Satoshi Tanaka, Kohji Yoshikawa, Takashi Minoshima, and Naoki Yoshida. Multidimensional Vlasov–Poisson simulations with high-order monotonicity- and positivity-preserving schemes. *The Astrophysical Journal*, 849(2):76, 2017. doi: 10.3847/1538-4357/aa901f.

R. B. Torbert, J. L. Burch, T. D. Phan, M. Hesse, M. R. Argall, J. Shuster, R. E. Ergun, L. Alm, R. Nakamura, K. J. Genestreti, D. J. Gershman, W. R. Paterson, D. L. Turner, I. Cohen, B. L. Giles, C. J. Pollock, S. Wang, L.-J. Chen, J. E. Stawarz, J. P. Eastwood, K. J. Hwang, C. Farrugia, I. Dors, H. Vaith, C. Mouikis, A. Ardakani, B. H. Mauk, S. A. Fuselier, C. T. Russell, R. J. Strangeway, T. E. Moore, J. F. Drake, M. A. Shay, Yuri V. Khotyaintsev, P.-A. Lindqvist, W. Baumjohann, F. D. Wilder, N. Ahmadi, J. C. Dorelli, L. A. Avanov, M. Oka, D. N. Baker, J. F. Fennell, J. B. Blake, A. N. Jaynes, O. Le Contel, S. M. Petrinec, B. Lavraud, and Y. Saito. Electron-scale dynamics of the diffusion region during symmetric magnetic reconnection in space. *Science*, 362(6421):1391–1395, 2018. ISSN 0036-8075. doi: 10.1126/science.aat2998.

T. Trost, S. Lautenbach, and R. Grauer. Enhanced conservation properties of Vlasov codes through coupling with conservative fluid models. *ArXiv e-prints*, page arXiv:1702.00367, 2017.

Liang Wang, Ammar H. Hakim, A. Bhattacharjee, and K. Germaschewski. Comparison of multi-fluid moment models with particle-in-cell simulations of collisionless magnetic reconnection. *Physics of Plasmas*, 22(1):012108, 2015. doi: 10.1063/1.4906063.

Masaaki Yamada, Jongsoo Yoo, Jonathan Jara-Almonte, Hantao Ji, Russell M. Kulsrud, and Clayton E. Myers. Conversion of magnetic energy in the magnetic reconnection layer of a laboratory plasma. *Nature Communications*, 5(1):4774, 2014. ISSN 2041-1723. doi: 10.1038/ncomms5774.